International Journal of Plasticity 83 (2016) 1–18

Contents lists available at ScienceDirect

International Journal of Plasticity

journal homepage: www.elsevier.com/locate/ijplas

Assessment of X-ray diffraction and crystal plasticity lattice strain evolutions under biaxial loading

T.O. Erinosho [a, *], D.M. Collins [b], A.J. Wilkinson [b], R.I. Todd [b], F.P.E. Dunne [c]

[a] Department of Mechanical Engineering, University of Bristol, BS8 1TH, United Kingdom
[b] Department of Materials, University of Oxford, Oxford, OX1 3PH, United Kingdom
[c] Department of Materials, Imperial College London, SW7 2AZ, United Kingdom

ARTICLE INFO

Article history:
Received 25 November 2015
Received in revised form 3 March 2016
Available online 5 April 2016

Keywords:
C. Finite element
B. Crystal Plasticity
A. Microstructures
X-ray diffraction

ABSTRACT

A methodology to simulate X-ray diffraction lattice strains using crystal plasticity, replicating in-situ synchrotron experimental measurements during the deformation of a low-carbon steel, has been developed. Uniquely, the model calculated lattice strains for full Debye–Scherrer diffraction rings, providing the in-plane lattice strain distributions determined from crystal plasticity. Thus, a direct method of comparison between experimental and crystal plasticity results becomes possible. The model considered two forms of hardening whilst subjecting the material to two dissimilar proportional strain-paths; uniaxial and balanced biaxial deformation. Both deformation paths showed influence on resulting lattice strain distributions which were also found to depend upon texture. Biaxial straining led to a stronger dependence on the material's hardening behaviour and this was attributed to the higher rate of work hardening seen under biaxial compared to uniaxial straining. However, biaxial deformation showed quite isotropic lattice strains distribution, irrespective of initial texture or hardening. Quantitatively, good agreement between the computed and experimentally determined lattice strain distributions was obtained for each strain path. This success demonstrates the possibility of calibrating crystal plasticity model parameters using such methodologies, or simply to provide insight into the governing mechanisms in polycrystal deformation.

1. Introduction

A framework to link X-ray diffraction lattice strain measurements with crystal plasticity finite element analyses is presented. The paper develops a virtual X-ray diffraction methodology which captures the experimentally measured deformation response to investigate the effects of texture on lattice strains developed under proportional strain-paths. The goal is to understand the evolution of lattice strains for differing deformation histories which is potentially useful in the design and optimisation of fabrication processes for metallic materials.

There are several materials characterization techniques used to determine lattice strain distributions in metals. Examples of such techniques include electron back-scattered diffraction (EBSD), X-ray and neutron diffraction (Cullity and Stock). Of particular interest to this study is X-ray diffraction which has a wide range of applicability in the understanding of

* Corresponding author.
E-mail addresses: t.erinosho12@imperial.ac.uk, tomiwa.erinosho@oxon.org (T.O. Erinosho).

http://dx.doi.org/10.1016/j.ijplas.2016.03.011

polycrystalline metals (Cullity and Stock). Two X-ray diffraction configurations that can be adopted include near and far field techniques which depend on the distance of the sample to the detector (Nervo et al., 2014). The near field configuration of diffraction is used to map grain morphologies and orientations while the far field method enables determination of strain distributions as well as orientations whilst neglecting grain morphology (Wong et al., 2013).

In both cases, an incoming X-ray probes the grains within the material which diffract if the Bragg condition is satisfied. For experiments at high energy synchrotron sources with a monochromatic beam energy, measurements can be obtained in transmission. As Bragg's law may be satisfied for a number of crystal orientations, the X-rays diffracted from a common lattice plane will form a cone with an angle 4θ at the apex. Using a position sensitive area detector, the X-ray intensity at the intersection of the diffracted cone is acquired; observed as a series of rings, often termed Debye–Scherrer rings, associated with each lattice plane. Analysis of these rings provides useful insight into the interplanar spacings within the material. Such measurements can be readily converted to a lattice strain with knowledge of a reference interplanar spacing. However, there are two inherent assumptions associated with the technique. First, it is assumed that the number of grains diffracting within the probed volume is sufficiently large to provide a statistical representation of the lattice strains within the material. This assumption is valid if the diffraction spots from individual grains cannot be distinguished. When considering lattice strains, the measurements are only valid when data is acquired from many grains to be representative of the bulk material response. Second, lattice planes that do not satisfy the Bragg condition remain invisible, leading to a loss of information. Again, a continuous ring increases confidence that a representative strain state for all crystallographic orientations has been obtained. Regardless of the limitations, the X-ray diffraction technique remains a useful method of characterizing sample orientation dependent lattice strain distributions within metals which is evident from the extensive literature available on the subject. It has been used to study fusion welding (Withers et al., 2008), residual stresses (Pagliaro et al., 2009; Cihak et al., 2006; Dye et al., 2003; Webster et al., 2001), deformation substructure (Korsunsky et al., 2010), cracks (Oddershede et al., 2012) etc. However, this paper focuses on the computational approaches developed so far for the simulation of X-ray diffraction.

Many researchers e.g. (Wong et al., 2013; Obstalecki et al., 2014; Barton and Dawson, 2001; Miller et al., 2008; Efstathiou et al., 2010; Demir et al., 2013; Park et al., 2013; Pellereau et al., 2010; McNelis et al., 2013; Dawson et al., 1998) have led studies on developing computational approaches for predicting diffraction patterns. Dawson and co-workers (Wong et al., 2013; Obstalecki et al., 2014; Miller et al., 2008; Efstathiou et al., 2010; Dawson et al., 1998) have adopted simulated X-ray diffraction as an auxiliary tool in design processes. For example, this technique has been used to investigate the sensitivity of a grain to its neighbourhood (Wong et al., 2013; Efstathiou et al., 2010). The effect was studied using two grains which were randomly placed at different positions within a polycrystal and their lattice strain and orientation recorded using the simulated far field X-ray diffraction. This enabled the extraction of microstructure sensitive data, providing insight into the initiation of strain localization. Dawson and co-workers have also employed this technique to investigate fatigue crack initiation (Obstalecki et al., 2014). Simulated X-ray diffraction patterns were shown to be useful in further understanding elastoplastic deformation that occurs within a polycrystalline aggregate leading to microcrack initiation. In this approach, diffraction analysis was undertaken on individual grains satisfying the diffraction condition.

Here, an understanding of the coupling between texture and hardening and the resulting lattice strain distributions under proportional straining is presented. Firstly, the experimental and crystal plasticity methods adopted are described in Sections 2 and 3 respectively, followed by a description of the virtual diffraction experiment in Section 4. Section 5 provides systematic studies of experimental and simulated diffraction polycrystal textures, followed by a discussion of these results in Section 6. Conclusions are presented in Section 7.

2. Experimental

Diffraction data were collected on the high energy beamline, I12 (Drakopoulos et al., 2015) at Diamond Light Source whilst deforming specimens in-situ. Specimens of a low carbon ferritic steel were deformed using a specially designed biaxial loading mechanism that fits onto a conventional tensile load frame; in this case a 10 kN Shimadzu AGS-X rig. The load frame was placed on a sample stage with the ability to translate in orthogonal directions, permitting its alignement with the incident X-ray beam. The sample stage also has the ability to rotate, however, measurements were restricted to normal incidence alone due to (i) a geometrical restriction from the biaxial mechanism that limits a rotation to ~+/− 20° without obscuring the beam path, and (ii) a limited ability to locate the centre of rotation (due to constraint (i)); necessary for accurate lattice spacing determination. The specimens were of a cruciform shape with a locally reduced thickness (from 1 mm down to 400 μm) at the centre of the specimen, creating a stress concentration at this location. The deformation state in this region was determined by the ratio of displacements applied by the mechanism, and the deformation rate controlled by the crosshead displacement of the load frame. As the deformation in the locally thinned region is of interest, the X-ray beam was aligned with the centre of this region, and hence all diffraction data were acquired from this region. Diffraction patterns were acquired at a rate of 0.25 Hz in combination with a cross head displacement rate of ~0.03 mm s^{-1}. The lattice strain evolutions of two strain-ratios were considered: (1) uniaxial deformation, and (2) biaxial deformation. Further details of the experimental configuration including specimen parameters can be found in Collins et al. A schematic of the experimental setup is shown in Fig. 1 (a) which presents the configuration of the biaxial load frame in relation to the incident X-ray beam and transmitted X-ray diffraction patterns. Radiographic images were also acquired at intervals during the deformation using an X-ray imaging camera shown upstream from the area detector. The radiographs were collected with a beam size of 10 × 10 mm, allowing the central region of the cruciform to be imaged. As the cruciform specimen geometry has regions of

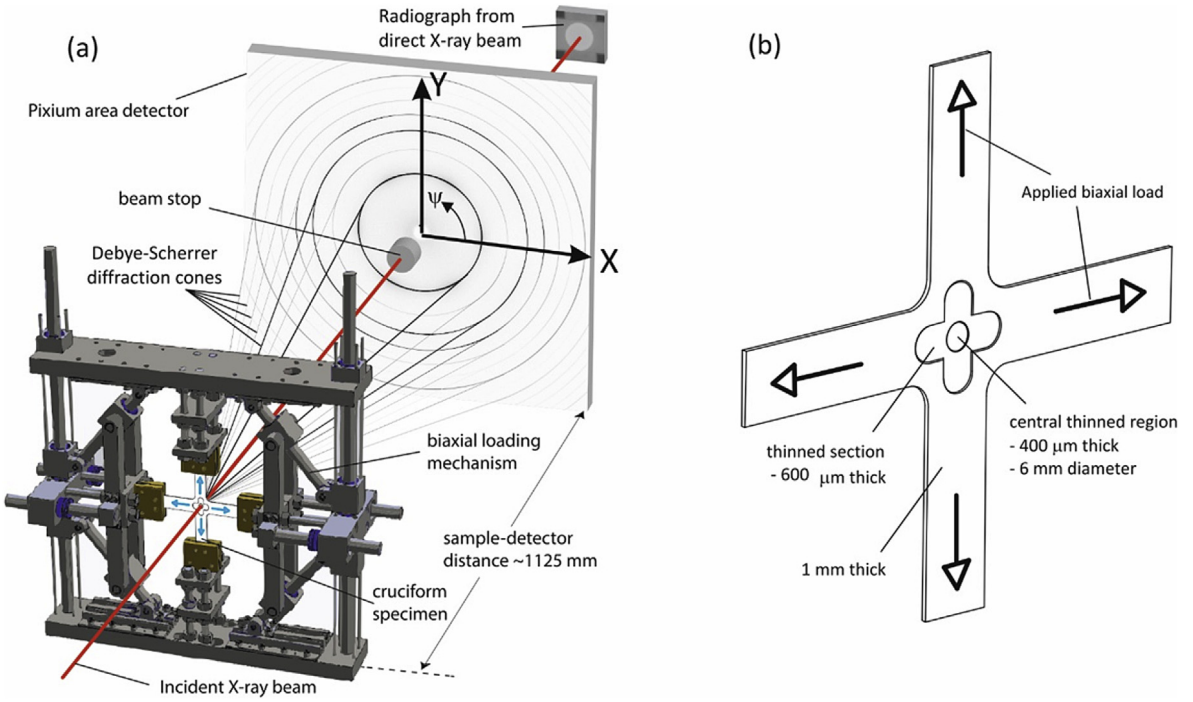

Fig. 1. (a) Experimental setup of diffraction experiment on I12, Diamond Light Source, and (b) a schematic of the cruciform sample design.

different thickness, as shown in Fig. 1 (b), regions that are thinnest appear brightest. The central region of interest was measured using this property with digital image correlation; radiographs during increments of loading were analysed to resolve the macroscopic strain in the X and Y directions.

Cruciform specimens were placed ~1125 mm from the Thales Pixium RF4343 2D area detector, which has a 2880 × 2881 X-ray sensitive array of pixels, of size 148 μm. This configuration permitted full Debye−Scherrer diffraction rings to be collected up to N = 10 where $N = h^2 + k^2 + l^2$ for lattice plane *hkl*. The monochromatic X-ray beam was calibrated using a CeO_2 standard in conjunction with a fitting routine described by Hart et al. (2013). To ensure a sufficient number of diffracted grains were measured, diffraction spectra were summed in a 4-point square-grid pattern, such that each adjacent illuminated volume had no overlap. This involved moving the sample relative to the beam, so that different grains from the specimen were sampled. During the deformation of the cruciform specimen, the region of interest moves upwards in the direction of the load frame crosshead. To compensate for this and to ensure the X-ray beam remained in the centre of the specimen, the entire load frame was displaced downwards on the sample stage at approximately half of the rate of the load frame crosshead. A monochromatic X-ray beam was used with a fixed energy of 90.36 keV and with an incident beam size of 0.5 × 0.5 mm. The short wavelength of the experiment means that the diffracting lattice planes provide measured d-spacings and lattice strains that are approximately in the sheet of the specimen. The high energy also has sufficiently low attenuation in the steel specimens used to enable the collection of diffraction patterns in transmission. Following data collection, each diffraction pattern was radially integrated into 36 sectors of equal spacing using the software FIT2D (FIT2D manual, 2014). Data from each sector provides intensity versus diffraction angle, 2θ. An example of this is shown in Fig. 2 with (a) an 2D experimental diffraction pattern and (b) a plot of the integrated data for a sector at an azimuthal angle $\psi = 0^\circ$ (i.e. parallel to X). Using this integrated data, analysis fitting routines were subsequently performed using MATLAB, with each of the reflections fitted with a pseudo-Voigt function. By monitoring the change in peak position during deformation with respect to a strain free reference, lattice strains were calculated. By repeating this process for each reflection for all sectors, lattice strain distributions were deduced.

The initial material pedigree was characterised using electron backscatter diffraction (EBSD) to provide the initial texture and the grain size distribution. A JEOL-6500F scanning electron microscope equipped with a TSL/EDAX OIM v6 EBSD system was used, operating with a beam current of 14 nA and an accelerating voltage of 20 keV. The collected data were acquired across a region 900 μm × 900 μm using a step size of 0.5 μm. Each diffraction pattern was indexed using a fitting routine of the Kikuchi bands in Hough space to provide the spatially resolved map of crystal orientations.

3. Crystal plasticity framework

The classical crystal plasticity framework based on the kinematic decomposition of the deformation gradient ($\boldsymbol{F}$) into elastic ($\boldsymbol{F}^*$) and plastic ($\boldsymbol{F}^p$) tensors as laid out by Lee (Lee, 1969) is adopted here such that

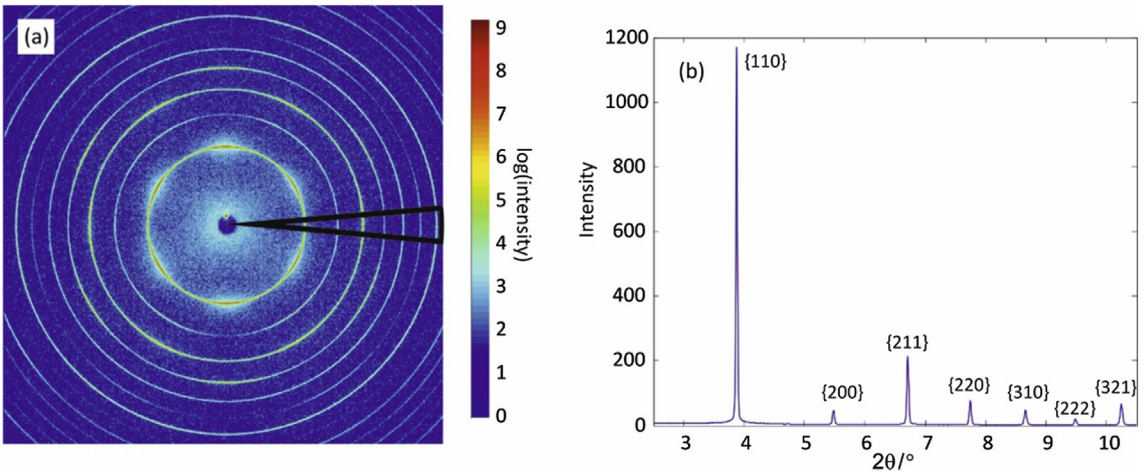

Fig. 2. (a) Example of experimental diffraction pattern with one sector outlined and (b) this sector radially integrated to provide intensity versus diffraction angle, 2θ.

$$\boldsymbol{F} = \boldsymbol{F}^{*}\boldsymbol{F}^{\mathrm{p}}. \tag{1}$$

The reader is referred to previous studies by Erinosho et al. (2013a, 2013b) which provide a detailed description of this framework. A power law constitutive rule relates the slip rate and resolved shear stress for a given slip system given by

$$\dot{\gamma} = \dot{\gamma}_0 \left|\frac{\tau^{\alpha}}{g^{\alpha}}\right|^{n} \mathrm{sgn}(\dot{\gamma}) \tag{2}$$

where the slip rate ($\dot{\gamma}^{\alpha}$) on individual slip system (α) depends on the reference strain rate, $\dot{\gamma}_0^{\alpha}$, resolved shear stress, τ^{α}, and slip system strength, g^{α}. Full details of this model may be found in Peirce et al. (1983) and Huang (1991). The hardening law and the slip system strength evolution is given by McGinty and McDowell (2004).

$$\dot{g}^{\alpha} = h_0 \left(1 + \frac{h_0 \gamma_{\mathrm{sum}}}{\tau_0 m}\right)^{m-1} \dot{\gamma}^{\alpha} \tag{3}$$

in which the accumulated slip is calculated from

$$\gamma_{\mathrm{sum}} = \sum_{\beta=1}^{N_{\mathrm{slip}}} \left(\int_0^t \dot{\gamma}^{(\beta)} dt \right). \tag{4}$$

Note that N_{slip} denotes the number of slip systems. The hardening modulus h_0, and parameter m for the particular material being investigated are adopted from Erinosho et al. (2013b) and are shown for the ferritic steel considered in Table 1. The experimental macroscopic response of the DX54 material when subjected to uniaxial loading is shown in Fig. 3 and the crystal plasticity hardening parameters adopted to compare simulations with experiment were obtained from earlier work by Erinosho et al. (2013a, 2013b) on similar steel to DX54 presented in Fig. 3. This is demonstrated by the comparable lattice strain responses presented and discussed later in this work.

Two extreme forms of hardening are considered here illustrated by their mechanical responses under uniaxial straining shown in Fig. 4. One form termed isotropic latent hardening has been adopted such that all slip systems, active or otherwise, undergo the same level of hardening. The slip resistance is assumed to be the same for all slip systems and corresponds to the maximum resistance currently developed, so that $\dot{\gamma}^{\alpha}$ in Eq. (3) is specified to be $(\dot{\gamma})_{\mathrm{max}}$, the maximum slip rate developed on any of the active slip systems. The other form of hardening considered is referred to as self-hardening such that only active slip systems undergo hardening, but independently Hence, unlike isotropic hardening, $\dot{\gamma}^{\alpha}$ in Eq. (3) depends on the slip rate

Table 1
Material properties of ferritic steel adopted from Erinosho et al. (2013b).

Model parameters								Experiment	
C_{11} (GPa)	C_{12} (GPa)	C_{44} (GPa)	n	m	$\dot{\gamma}_0$ (s^{-1})	τ_0 (MPa)	h_0 (GPa)	YS (MPa)	TS (MPa)
231.4	134.7	116.4	40	0.245	1	110	0.9	140–300	270–450

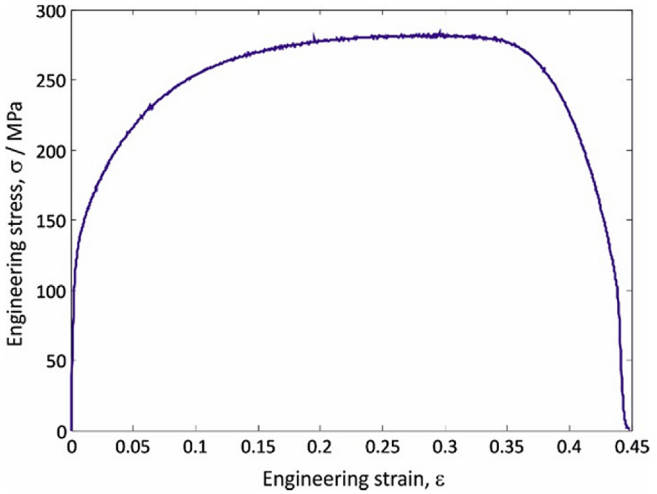

Fig. 3. Experimental uniaxial tensile response of DX54 steel to failure.

on that particular slip system and the accumulated slip summed over all slip systems. It is seen from Fig. 4 that isotropic hardening results in a higher flow stress with increasing deformation compared to self-hardening. This is attributed to the more uniform nature of hardening scaled to the maximum slip rate in the isotropic case such that slip systems active or otherwise undergo the same levels of hardening as opposed to self-hardening. The CRSS (τ_0) detailed in Table 1 was chosen in order for the mechanical responses for both isotropic and self-hardening to fall within the experimentally observed limits of yield and tensile strengths illustrated in Fig. 4.

Note that the 24 BCC slip systems comprising 12 {110}<$\bar{1}$11> and 12 {112}<$\bar{1}\bar{1}$1> families are considered in this study with the model parameters for slip on {110} and {112} taken to be the same. Previous studies by the authors have shown that using 24 slip systems does not greatly affect the predicted stress states or dislocation distributions (Erinosho et al., 2013b). Further, Lewis et al. (2010) showed the effects of incorporating the twelve (112)<111> systems as against twenty-four (123)<111> slip systems in texture prediction is not significant if only the (110)<111> family are used. In addition, the strains considered here are relatively small (~5%) and hence, the incorporation of the full set of 48 BCC slip systems is likely to be minimal. Strain rate effects have also been minimised since they are likely to be small at room temperature for the ferritic steel considered and a high value of rate sensitivity parameter, n, in the slip rule Eq. (2), has been chosen appropriately for this purpose.

The crystal plasticity finite element approach adopted here is chosen because it accounts for grain constraint effects as well as strong variations (e.g. in orientation) which develop intragranularly. Self-consistent models on the other hand are limited in accounting for local effects (eg see Warwick et al. (2012a, 2012b)) but can provide an excellent representation of average stress-strain behaviour. Since it is important in this work to capture the intragranular representation of lattice orientation, slip and strain, a crystal plasticity finite element methodology is preferred.

4. X-ray diffraction modelling

The X-ray diffraction methodology used to calculate virtual diffraction patterns using crystal plasticity is presented here. Consider Fig. 5 which shows an X-ray incident on a single crystal of known crystallographic orientation leading to diffracted beams which are recorded on a detector as shown. Each plane that satisfies Bragg's condition diffracts X-rays to the detector.

Each lattice plane, (hkl), is described by its plane normal in its local crystallographic configuration in the deformed state. This vector, $\mathrm{r}_{\mathrm{hkl}}$, is given by

$$\mathrm{r}_{hkl} = \Delta \boldsymbol{R}^{\mathrm{c}} \boldsymbol{R}_0^{\mathrm{c}} \begin{pmatrix} h \\ k \\ l \end{pmatrix} \tag{5}$$

where $\boldsymbol{R}_0^{\mathrm{c}}$ is a rotation matrix which maps the undeformed crystal from the reference state to the local crystallographic configuration and $\Delta \boldsymbol{R}^{\mathrm{c}}$ maps the local crystal orientation into the deformed state. The forward projection (s_0) of the diffracted beam onto the detector XY plane is given by

$$s_0 = \frac{1}{\sqrt{[\mathrm{r}_{hkl}(1)]^2 + [\mathrm{r}_{hkl}(2)]^2}} \begin{pmatrix} \mathrm{r}_{hkl}(1) \\ \mathrm{r}_{hkl}(2) \\ 0 \end{pmatrix} \tag{6}$$

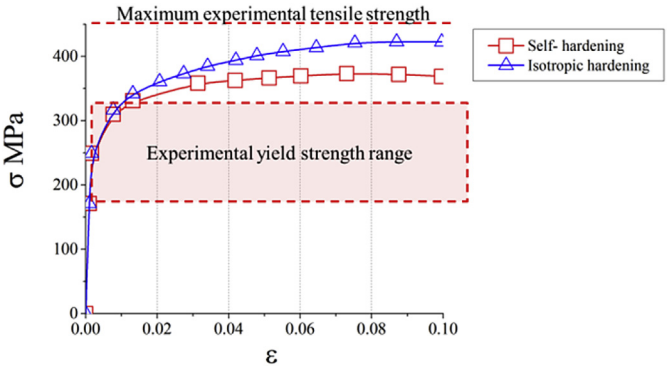

Fig. 4. Mechanical stress strain response based on calibration of CRSS to experimental data (Erinosho et al., 2013b).

where $r_{hkl}(1)$ and $r_{hkl}(2)$ represent the X and Y components of the rotated (hkl) plane respectively. From Bragg's law, the angle of diffraction, θ_b, is given by

$$\theta_b = \sin^{-1}\left(\frac{\lambda}{2d_{hkl}}\right) \tag{7}$$

where λ is the wavelength of the incoming X-ray beam and d_{hkl} is the interplanar spacing of a plane with normal hkl. Assuming λ is small, typical of synchrotron diffraction, $\theta_b \approx 0$ and, diffraction is satisfied when $\theta_b = \theta_0$ where $\theta_0 = \cos^{-1}\{s_0 \cdot r_{hkl}\}$. In the experiment instrumental line broadening effects determine whether the crystal, or a fragment of it, is in the correct orientation to diffract, while in the simulations a tolerance can be set allowing some deviation from the exact Bragg condition to replicate this effect. Throughout this study, this tolerance was set to 5° which is significantly larger than in the experimental case and is set to improve statistics while not being so large as to include grossly different mechanical states. That is, contributions to the virtual diffraction pattern are recorded when $\theta_b - 5^\circ < \theta_0 < \theta_b + 5^\circ$ and the azimuthal angle of the diffracted beam on the area detector, ψ, subsequently denoted as the rotation from X shown schematically in Fig. 6 (b) is calculated using

$$\Psi = \tan^{-1}\left(\frac{r_{hkl}(2)}{r_{hkl}(1)}\right). \tag{8}$$

Each diffraction spot recorded on the detector corresponds to a plane within a crystal (or element within the computational framework) and contains information on its crystallographic orientation as well as the lattice strain. Assuming the crystal is unstrained and the detector is orthogonal to the beam, the resulting Debye Scherrer ring (for a range of crystals) recorded at the detector will be circular and is regarded as the reference. Now, if the crystal shown in Fig. 5 has an inherent strain, the change in interplanar spacing results in a shift of the corresponding diffraction spot. This results in a distorted Debye Scherrer ring, indicating the presence of strain in a particular family of planes. Typically, this will vary as a function of the macroscopic deformation. The result for each deformed state is a series of rings corresponding to each diffracting plane family i.e. {110}, {200}, {310} etc. as illustrated in Fig. 6 (a). For simplicity, consider the {310} family shown in Fig. 6 (b). In the undeformed state, the resulting Debye Scherrer ring has a uniform radius; however, upon (e.g.) uniaxial deformation, the radius of this ring changes, becoming elliptical with major and minor axes linked to the in plane principal elastic strains Consecutive diffraction rings are compared to evaluate differences in radius for azimuthal sectors (illustrated in Fig. 6 (b)) around the ring and then recorded as a function of the overall macroscopic applied strain in order to obtain the evolution of elastic strains over the whole deformation history.

Fig. 6 (b) shows a schematic of azimuthal sectors such that all diffracting beam intensities which fall within the highlighted sector (with knowledge of the associated lattice spacing calculated from crystal plasticity) in the series of diffraction images are binned and the average lattice spacing for that particular azimuthal sector is then obtained. This activity is equivalent to the experimental processing method shown in Fig. 2. This process is first carried out on the diffraction rings of the unstrained sample to obtain the reference lattice spacing, d_0^j, for each azimuthal sector. This corresponds to the theoretical d_0 for a particular family of planes. Subsequently, the process is repeated for the Debye Scherrer rings corresponding to the deformed sample to obtain d_i where $i = 1, 2, 3 \ldots n$ represents deformation states 1, 2, 3 … n. The lattice strain (ε_{lat}) is then calculated for each azimuthal sector j at deformation state i using

$$\varepsilon_{lat}^j = \frac{d_i^j - d_0^j}{d_0^j}. \tag{9}$$

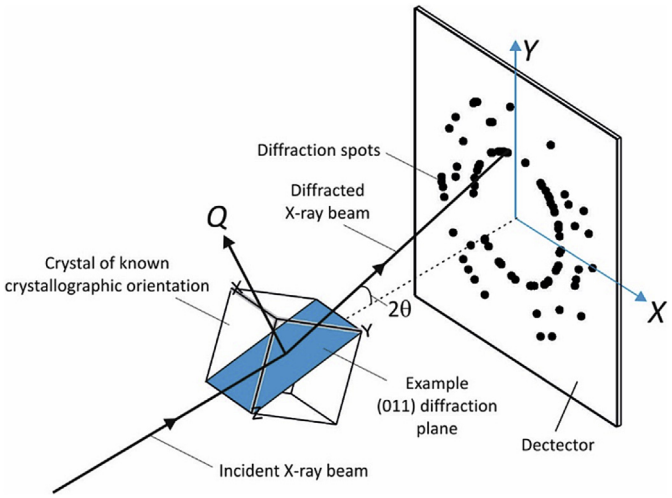

Fig. 5. Schematic of the computational approach used to simulate X-ray diffraction patterns using the crystal orientations simulated in the crystal plasticity finite element model.

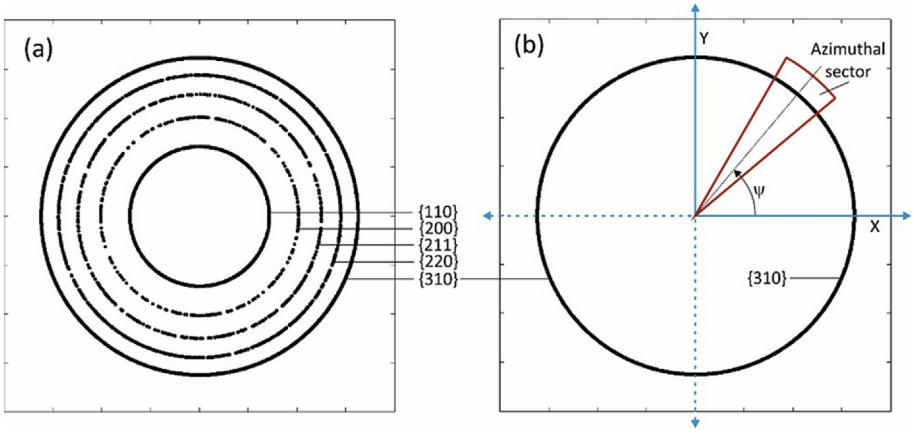

Fig. 6. Schematic of simulated Debye–Scherrer rings corresponding to a particular deformation state. (a) Shows the rings corresponding to diffraction from the 5 lattice planes with the lowest *hkl* indexin BCC ferritic steel and (b) illustrates the binning of azimuthal sectors using an example {310} diffraction ring.

Note that ε_{lat} corresponds to a particular family of planes and can be calculated for the {110}, {200}, {211}, {310} etc. families independently. Further, ε_{lat} is elastic in origin i.e. it is an indication of the elastic strains developed during deformation. Hence, the post deformation lattice strains due to elastic distortions are calculated within the crystal plasticity finite element framework using the methodology presented by Erinosho and Dunne (2014). This technique calculates an element by element lattice strain corresponding to each particular plane within the family of planes present (i.e. {110}, {200}, {211}, {310}) by using the elastic deformation tensor $\boldsymbol{F}^*$ such that

$$\frac{a}{a_0} = |\boldsymbol{F}^* \boldsymbol{e}_1^c|, \frac{b}{b_0} = |\boldsymbol{F}^* \boldsymbol{e}_2^c|, \frac{c}{c_0} = |\boldsymbol{F}^* \boldsymbol{e}_3^c| \tag{10}$$

where $a_0 = b_0 = c_0 = 2.880$ Å (Cullity and Stock) are the undeformed lattice lengths and $\boldsymbol{e}_1^c$, $\boldsymbol{e}_2^c$ and $\boldsymbol{e}_3^c$ are unit orthogonal vectors rotated into the deformed crystallographic configuration. That is,

$$\boldsymbol{e}_i^c = \Delta \boldsymbol{R}^c \boldsymbol{R}_0^c \boldsymbol{e}_i \tag{11}$$

where $i = 1, 2$ and 3 corresponds to the [100], [010], and [001] directions respectively. Full details of the crystal orientation mappings can be found in Erinosho and Dunne (2014). With knowledge of the deformed lattice lengths, the lattice spacing for all possible *hkl* planes in a BCC crystal can be obtained using Cullity and Stock.

$$d_{hkl} = \left(\sqrt{\frac{h^2}{a^2} + \frac{k^2}{b^2} + \frac{l^2}{c^2}} \right)^{-1}. \tag{12}$$

Thus, using Eq. (8), $d_0 = 0.9107$ Å for the {310} family of planes and similarly, $d_0 = 1.440$ Å for the {200} lattice planes, for example. The lattice strain ($\varepsilon^j_{\text{lat}}$) for each sector j illustrated in Fig. 6 (b) is then calculated using

$$\varepsilon^j_{\text{lat}} = \frac{\frac{\sum_{k=1}^{n_j} d^k_j}{n_j} - d_0}{d_0} \tag{13}$$

where $k = 1,2, \ldots n_j$. n_j is the total number of lattice planes that diffract within a particular sector j.

5. Results

5.1. Textures and finite element model

A subset of the collected EBSD inverse pole orientation data from which the initial texture was calculated is shown in Fig. 7 (a). The grains are shown to be approximately equiaxed with a unimodal grain size distribution as shown in Fig. 7 (b). The average grain size was measured to be 12.5 μm with a standard deviation of 8.6 μm. Representations of the textures adopted in this study are shown in Fig. 8. T-1 is a fully random texture obtained numerically. It was obtained by dividing the major and minor axes of a sphere into sectors which denote the number of random orientations of interest taking account of its associated asymmetry. Subsequently, the 3-D points in each sector are then projected onto the equator to obtain perfectly randomly distributed orientations.

T-2 (exp) is an experimentally measured ferritic steel texture obtained using electron backscatter diffraction (EBSD) and T-2 (sim) is a computational polycrystal representation of T-2 (exp) generated by sampling the orientations from the parent experimental texture. The orientation data was obtained from 2-D Electron Back Scattered Diffraction (EBSD) comprising thousands of grains including their $x - y$ coordinates to denote their location. Using this information, an average was obtained using an approach adopted similar to Raabe et al. (2002a, b) and Zhao et al. (2001). The process of mapping experimentally obtained texture components which have more grains, to the finite element simulation is done in two stages. The discretised orientation (mean) of each grain is first obtained followed by the progressive downsizing of experimental datasets to the number required for the model taking account of the area-weighted orientation distribution. Fig. 8 which compares the experimentally obtained pole figure for T-2 (comprising thousands of grains) with that generated from 512 grains used in the crystal plasticity simulation shows good agreement.

The polycrystal model adopted is shown in Fig. 9 with $8 \times 8 \times 8$ grains which are shown as regions of similar colour and a uniform mesh refinement ($6 \times 6 \times 6$ elements per grain) is adopted (See appendix A for a mesh sensitivity study). These cubic grains had dimensions $25 \times 25 \times 25 \mu m^3$. The boundary conditions are such that all faces are constrained to remain planar (see Appendix B for justification). Using the methodology described in Sections 3 and 4, the lattice strain is calculated for the {310} family of planes and presented against the azimuthal angle measured from the X-axis about the Debye Scherrer ring. An angular range of $\pm 5^\circ$ is adopted per azimuthal sector which is in-line with the angular tolerance from the Bragg condition used in constructing the virtual diffraction patterns, and as was also performed on the experimental diffraction patterns, giving 18 sectors about the Debye Scherrer ring. On this basis, the effects of texture and hardening on lattice strain distributions and their evolutions are presented next.

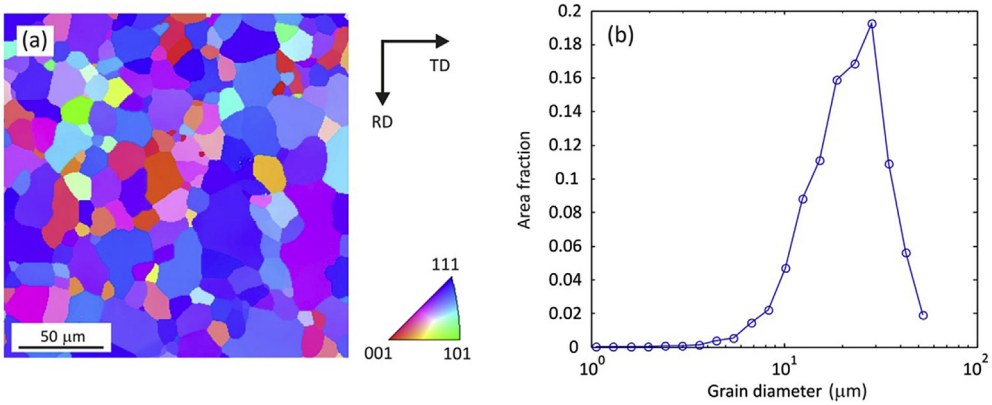

Fig. 7. (a) Electron backscatter diffraction inverse pole figure map of annealed DX54 steel, and (b) the corresponding grain diameter distribution.

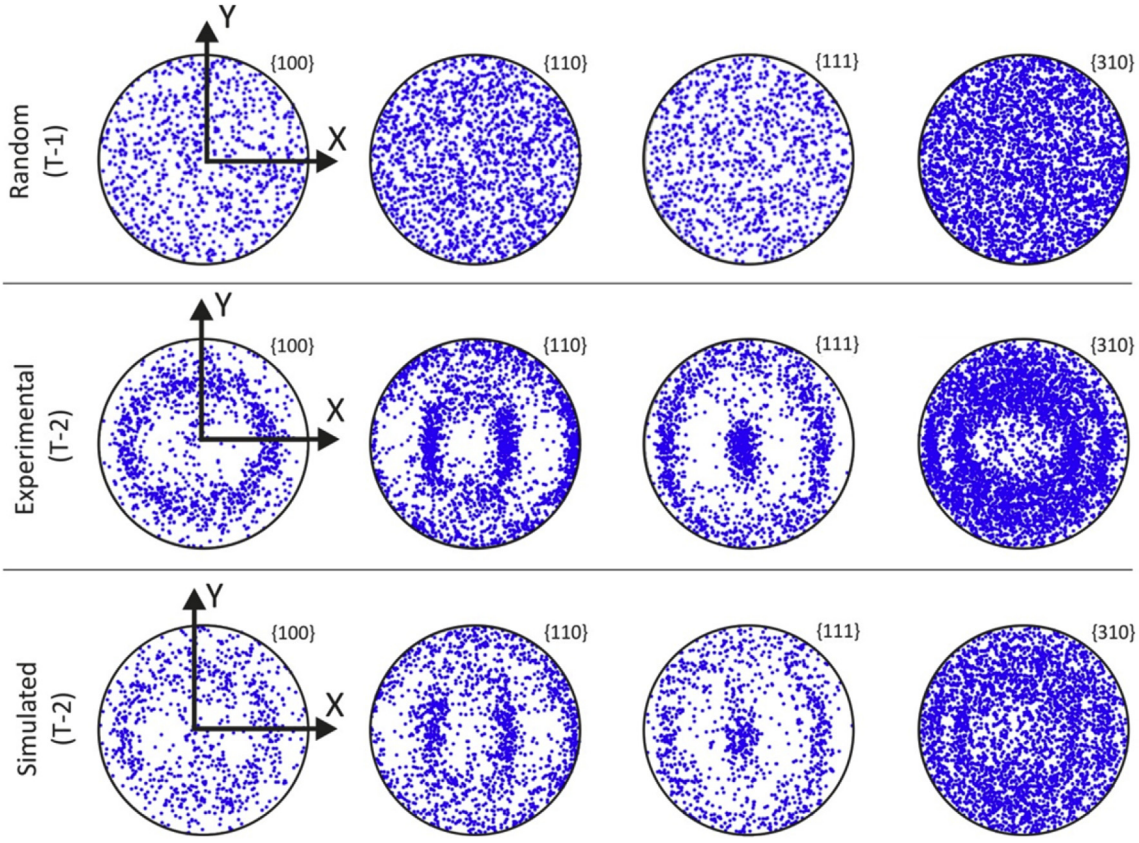

Fig. 8. Initial textures used in the simulations showing [T-1] a nominally random texture, [T-2(Exp)] an experimentally obtained ferritic steel texture and [T-2 (Sim)] a computational polycrystal representation of the texture [T-2 (Exp)].

5.2. Effects of texture and hardening on lattice strain distributions

This section addresses the lattice strain distributions obtained under differing deformation conditions. A description of the experimentally obtained results is presented first followed by detailed comparisons with the predicted lattice strains obtained from the crystal plasticity technique presented above.

Fig. 10 shows the experimentally measured lattice strains under biaxial (Fig. 10 (a)) and uniaxial (Fig. 10 (b)) deformation for the experimental texture T-2 shown in Fig. 8. Consider first Fig. 10 (a)which shows the lattice strains at 5% biaxial strain with $\varepsilon_Y = 0.05$. Though perfectly balanced biaxial deformation was targeted, i,e. $\varepsilon_Y/\varepsilon_X = 1$, anisotropic rig compliance meant that a strain ratio of $\varepsilon_Y/\varepsilon_X = 1.5$ was actually achieved. For this reason, a greater magnitude of lattice strain is observed at azimuthal angles, ψ, close to 90°, parallel to ε_Y. It is also noted that uniaxial deformation with the ideal strain ratio of $\varepsilon_Y/\varepsilon_X = -1/\nu$ was approximately achieved experimentally. However, some deviation from this would be expected due to the constraints imposed by the cruciform geometry, affecting the load transmitted across the central thinned section. In Figs. 10–12 the horizontal axis shows the macroscopic strain (ε_Y), while the vertical axis shows the azimuthal rotation, ψ, from the X-direction illustrated in Figs. 1 (a) and 6 (b). The colour scale indicates the measured lattice strain calculated from Eq. (9). It is apparent from Fig. 10 (a) that biaxial straining results in a relatively isotropic lattice strain distribution irrespective of the azimuthal angle. This implies the magnitude of lattice strain approximately in the plane of the specimen, is equivalent in all diffracting grains. Different behaviour is, however, seen under uniaxial loading along the Y-axis shown in Fig. 10 (b) whereby the lattice planes that diffract at 90° from the X-direction are noticeably in tension while those oriented away show progressively lower lattice strain, and compressive behaviour at orientations close to 0° and 180° from the X-direction.

Simulated X-ray diffraction results, calculated from the crystal plasticity approach, are also assessed. The model polycrystal textures shown in Fig. 8 are subjected to biaxial and uniaxial straining under the two forms of hardening (self- and isotropic) as described in Section 3. Fig. 11 shows the predicted lattice strain distribution for the {310} family of planes in random texture T-1 and experimental texture T-2 (sim) subjected to up to 5% biaxial straining under isotropic and self-hardening.

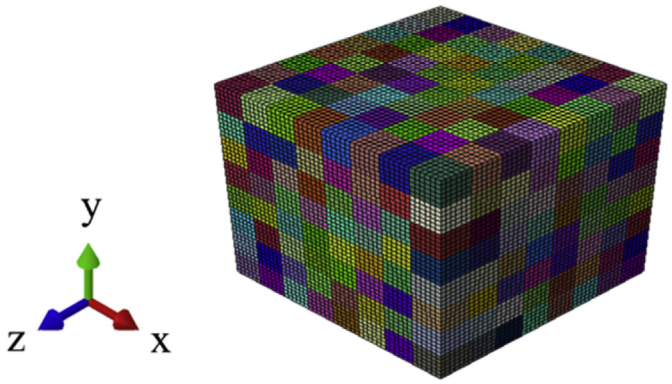

Fig. 9. The polycrystal model adopted with 8 × 8 × 8 grains. Note that the same mesh refinement (6 × 6 × 6 elements per grain) was adopted per grain in all oligocrystal models and each grain had dimensions of 25 × 25 × 25 μm^3. Note that colour denotes a region of uniform crystallographic orientation. (For interpretation of the references to colour in this figure legend, the reader is referred to the web version of this article.)

Random texture T-1 shows approximately uniform lattice strain irrespective of orientation (rotation from X-axis) as expected under both hardening forms. The apparent band between 60° and 120° results from the imbalanced nature of the biaxial straining adopted ($\varepsilon_Y/\varepsilon_X = 1.5$), thereby leading to preference for higher tensile lattice strain in this region. But, T-2 (exp) shows stronger variation in a similar region i.e. between 60° and 120°, due to the initial preference of its grains in the Y-direction. Moreover, a relatively uniform distribution is still observed regardless of orientation (rotation from X).

Fig. 12 shows the {310} lattice strain for random texture T-1 and experimental texture T-2 (sim) subjected to up to 5% uniaxial straining. Similar to the biaxial case, the lattice strain is shown along the deformation history for each azimuthal sector (rotation from X-illustrated in Fig. 6 (b). Consider first Fig. 12 (a1) and Fig. 12 (a2) which show the lattice strain for the initially random polycrystal texture under isotropic and self-hardening respectively. The band of higher lattice strain seen between 60° and 120° shows that the subset of {310} family of planes which are normal to the Y-direction in Fig. 12 are experiencing higher net tensile strains, thereby leading to the band seen. However, due to texture, the band is less pronounced compared to the initially textured polycrystal T-2 (sim) whose lattice strains are shown in Fig. 12 (b). It is argued that the elastically stiff 111 plane normal directions in ferritic steel influence the magnitude of strain seen in Fig. 12 for both textures. From the pole figures shown in Fig. 8, it is clear that T-2 has more 111 plane normal perpendicular to the loading compared to the initially random texture T-1. Hence, fewer stiff 111 normals perpendicular to the tensile stress direction results in larger strains in that direction as seen.

Lastly, the lattice planes perpendicular to the loading direction which diffract close to 0° and 180° are, however, in compression as expected for both textures considered, and as observed in the experimental measurements in Fig. 10 (b).

6. Analysis and discussion

The aim of this study is to present comparison between simulated X-ray diffraction patterns, and those obtained from in-situ experimental measurements.

A cruciform specimen has been designed and used, specifically for the use with the biaxial loading mechanism and to permit suitable diffraction pattern acquisition. As stated previously, the central region of the specimen moves in the positive vertical direction with the displacement of the load frame crosshead. To ensure the incident beam remains in the gauge section of the specimen, the load from is moved vertically downloads. These movements cannot be perfectly synchronised; thus diffraction data will be collected from different grains if the sample is displaced relative the incident X-ray beam. This strategy can be mitigated if the diffracting grains are subjected to, on average, to the same macroscopic strain state. To monitor whether this assumption is suitable, diffraction patterns were collected as a map in the vicinity of the central thinned section of the specimen. The results of the spatially resolved {310} lattice strains are shown in Fig. 13 in two orthogonal directions (vertical direction, $\psi = 90°$ in (a) and horizontal direction, $\psi = 0°$ (b)). The maps interrogate a 10.5 × 10.5 mm^2 area with a step size of 0.5 mm step size in the vertical and horizontal directions. The beam size was 0.5 × 0.5 mm^2. This example map was acquired during the biaxial deformation with $\varepsilon_y = 0.07$ and $\varepsilon_x = 0.04$. The locally thinned region at the centre of the specimen can be identified with a {310} lattice strain of approximately 1.5 × 10^{-3}. The regions (i) and (ii) denote 3 × 3 mm^2 box, corresponding to the outermost limits that the beam probed during the deformation. This was confirmed with radiographs acquired at intervals during the deformation. From the range of lattice strains measured in each map plotted as a histogram, the subset of data from boxes (i) and (ii) are also displayed. These each show that a narrow distribution of lattice strains were measured in the gauge section of the specimen, and specifically in the region where data were acquired. The mean lattice strains were measured as 1.3 × 10^{-3} +/− 0.06 × 10^{-3} for $\psi = 0°$ and 1.2 × 10^{-3} +/− 0.04 × 10^{-3} for $\psi = 90°$, with the errors given as the standard deviation.

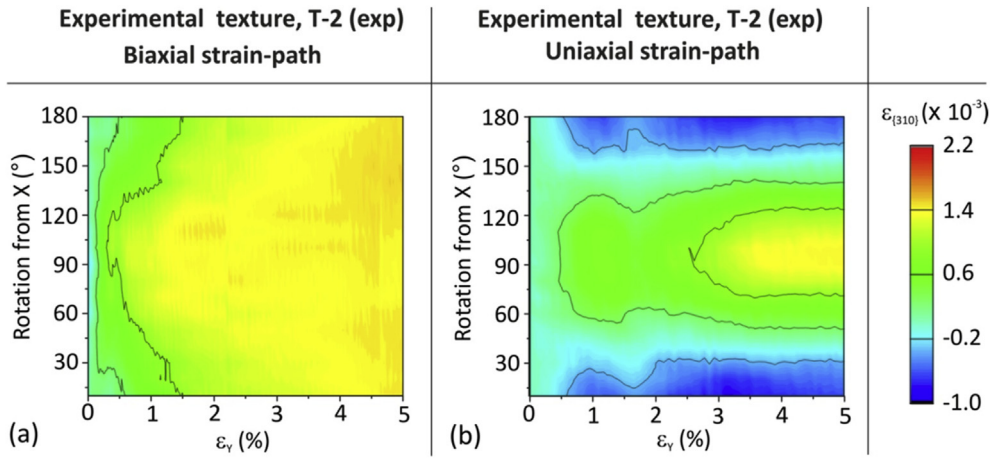

Fig. 10. Experimentally measured {310} lattice-strain during deformation subjected to biaxial (a) and uniaxial (b) strain-paths.

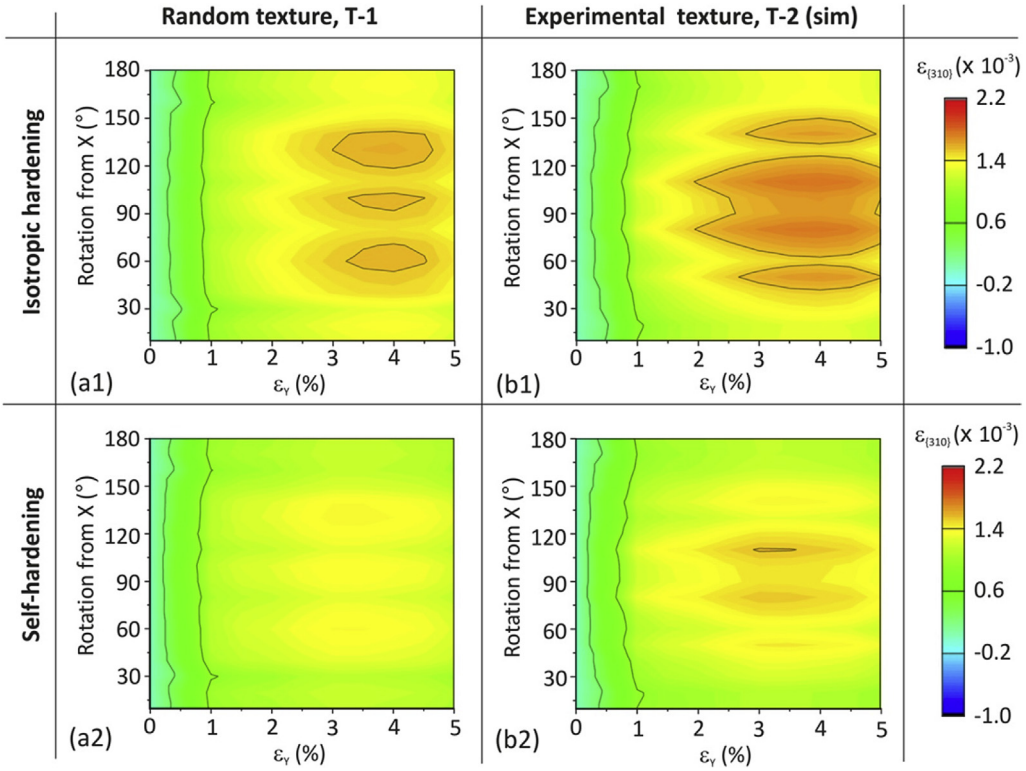

Fig. 11. Evolution of {310} lattice-strain for the random texture T-1 and experimental texture T-2 (sim) subjected to biaxial straining, calculated under isotropic (a1 & b1) and self-hardening (a2 & b2).

In the X-ray diffraction measurements, the diffracted beam recorded at the detector is a superposition of reflected beams from lattice planes within the diffraction volume. In the crystal plasticity model, however, a direct determination of lattice strain distributions for given slip system families is possible, so it is necessary to be aware of the differences which may arise from the inherent approximation being made in the X-ray measurement. In the crystal plasticity model, each material point is deemed a crystal with given orientation which interacts individually with the incoming simulated X-ray beam resulting in diffracted points if it satisfies the Bragg condition within a 5° tolerance. A higher tolerance was set for the model than applies in the experiment (~0.02°) due to the small number of grains that are likely to satisfy the Bragg condition in the model. The selected tolerance was deemed to be sufficiently small that all diffracting lattice planes, within a given

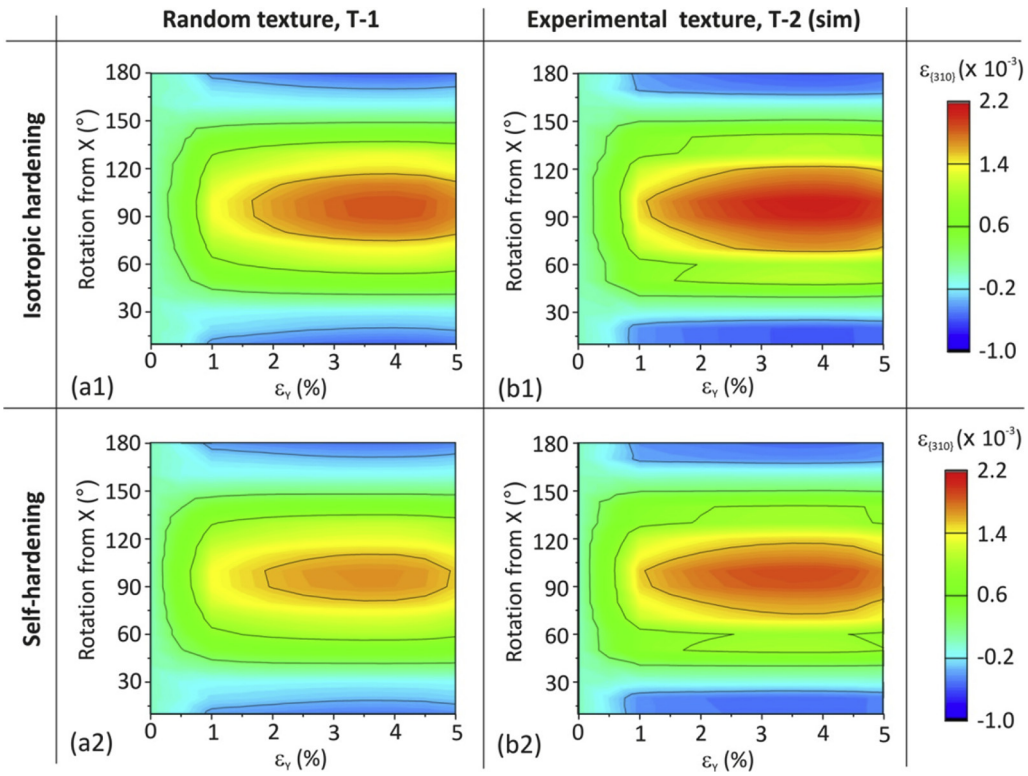

Fig. 12. Evolution of {310} lattice strain for random texture T-1 and experimental texture T-2 (sim) subjected to uniaxial straining under isotropic (a1 & b1) and self-hardening (a2 & b2).

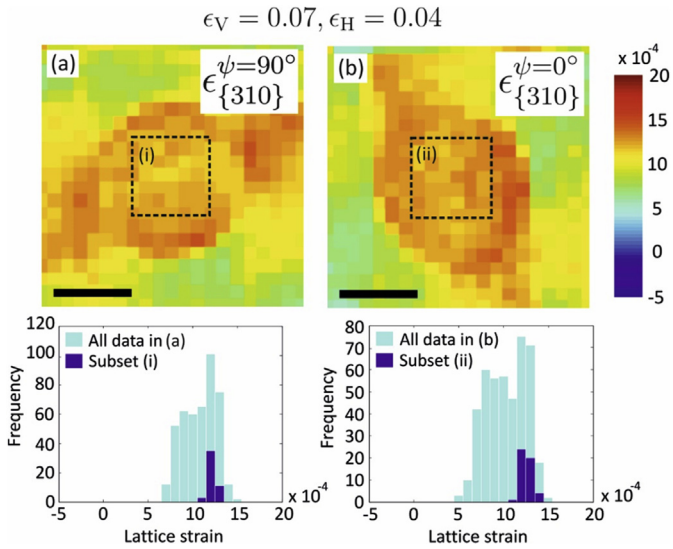

Fig. 13. (a) Map of {310} lattice strains in the vicinity of the central thinned region of the cruciform specimen at $\psi = 90°$ for an example biaxial deformation state. A histogram below shows the distributions of lattice strains for the full map and for the subset region (i). This is shown equivalently in (b) at $\psi = 0°$ with a histogram below including data from the subset region (ii).

azimuthal sector, were subjected to a similar stress state. This is equivalent to a small sample rotation, as shown to be necessary by Wong et al. (2013).

The computational time required to run a crystal plasticity model with the same number of grains that are illuminated by the X-ray beam in an experiment would be unrealistically long and prohibited by current computer hardware.

Assuming a sample thickness of 400 μm, the beam size, and a mean grain size of 12.5 μm, a crude estimate of ~$2 \cdot 10^5$ grains would be required in the volume. Clearly, this is much greater than the 512 ($8 \times 8 \times 8$) grains simulated in the present work. Macroscopically, the predicted stress-strain response is reliable, as shown in a previous study (Erinosho and Dunne, 2014). However, consideration of the micromechanics via lattice strain measurement is more difficult to validate.

From the experimental number of grains probed, a prediction can be made of the proportion of these grains that diffract. A simulation of 2×10^5 grains at random orientations with an arbitrary angular misorientation of 0.1° using an experimental tolerance for the Bragg condition (0.02° converts to an approximate bandwidth range of 90.2+/−0.2 keV) reveals that diffraction occurs from {310} lattice planes in approximately 5% of the grains. This is in comparison to <0.4% of grains diffracting from a lower multiplicity {200} lattice plane, for example. Therefore, multiplicity plays a key role in selecting the appropriate reflection for comparison between a simulation and experiment. Repeating this simple calculation for a Bragg tolerance of 5° predicts >75% of grains diffract from a {310} lattice plane. Whilst any reflection experimentally could be compared as seen in earlier works by Collins et al., the {310} lattice planes were used due to their high multiplicity. The likelihood of a crystal with a lattice plane from this family obeying Bragg's law is thus high, particularly when the Bragg angle is relaxed. With only a limited number of grains simulated, including information from lattice planes with a lower multiplicity would provide information from too few grains, which are therefore unlikely to be statistically representative of the experiment. Taking into account these factors, the simulated {310} lattice strain distributions compares well with the experimental results shown in Fig. 14, indicating the micromechanics are being accurately represented by the model. Fig. 14 compares lattice strain distributions at a macroscopic strain of 0.3% and 5% under biaxial and uniaxial straining. Whilst some differences exist between experiment and simulation (isotropic hardening) under both deformation paths, the simulation closely captures the distributions seen in the experiments.

The hardening law used in the simulation was also seen to influence the lattice strain distributions calculated. Under isotropic hardening, all slip systems undergo the same levels of hardening based on the maximum level of slip achieved, as illustrated in Eq. (3). Self-hardening conversely dictates that hardening on a slip system depends more significantly on the level of slip on that system alone. Hence, isotropic hardening is expected to result in greater hardening and consequently, higher lattice strains as seen in Figs. 11 and 12.

While isotropic hardening resulted in higher lattice strains due to the nature of hardening, the distributions observed were similar to those for self-hardening as seen in Fig. 15. But, biaxial straining showed a greater influence from the hardening law used compared to uniaxial loading. Considering the biaxial case shown in Fig. 15, it is clear that the form of hardening influences the behaviour evident in the distinct distributions of lattice strains seen for isotropic and self-hardening. This is attributed to the fact that the equivalent plastic strain rate under biaxial straining is twice that seen under uniaxial straining

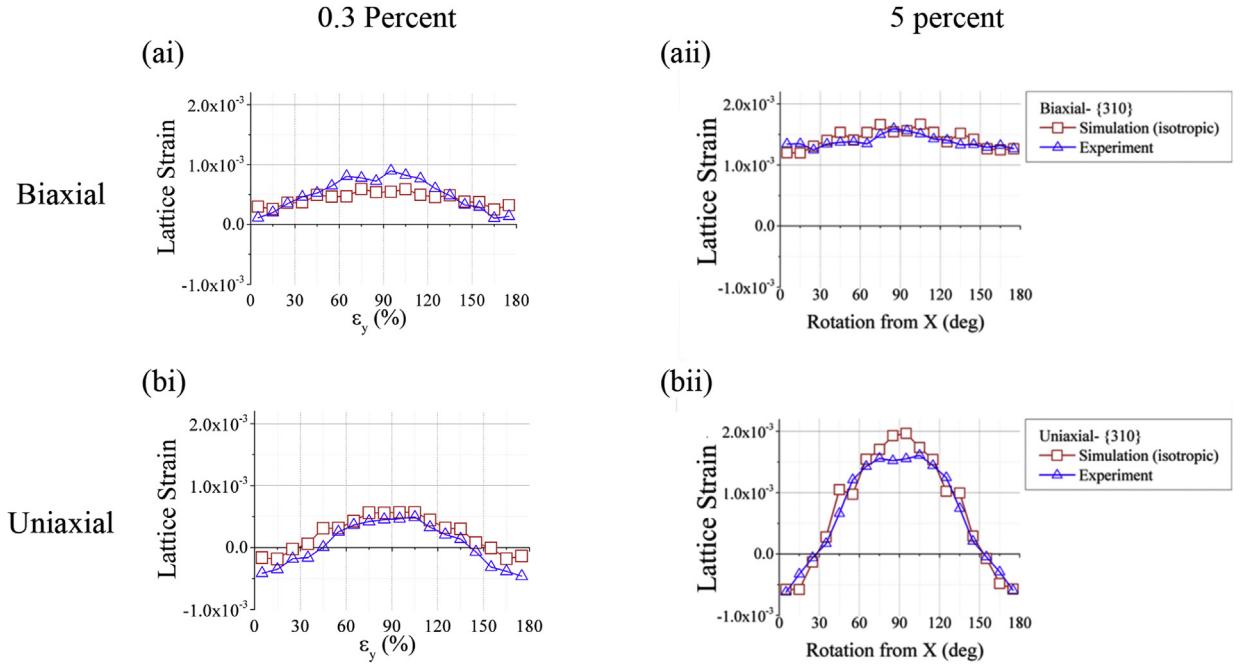

Fig. 14. Lattice strain at differing levels of uniaxial and biaxial straining for texture T-2.

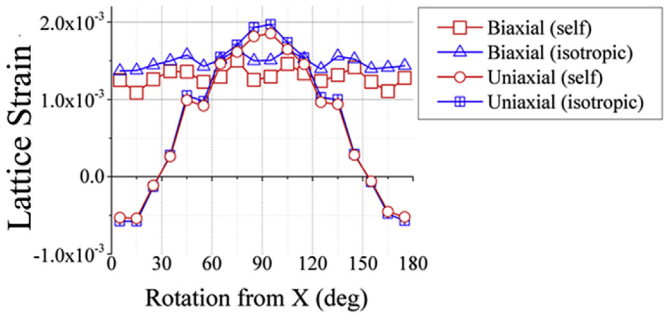

Fig. 15. Comparison of computed lattice strainfor uniaxial and biaxial strain-paths, each with $\varepsilon_Y = 5\%$, under isotropic and self-hardening.

further illustrated in Appendix C. Therefore, it is expected that the differences developed under biaxial straining based on the extreme forms of hardening adopted will be more pronounced compared to under uniaxial straining.

Further, the evolution of lattice strains under uniaxial and biaxial straining is compared in Figs. 16 and 17. Consider Fig. 16 (a) and (b) which compares the calculated evolution of lattice spacing under isotropic and self-hardening with experiment at 90° and 0° rotation from X respectively. Note that 90° corresponds to lattice spacing change parallel to the Y-direction in Fig. 6 (b) while 0° is parallel to the X-direction. The unbalanced biaxial nature discussed earlier (i.e.$\frac{\varepsilon_Y}{\varepsilon_X} = 1.5$) is immediately apparent given the relatively higher lattice spacing evolution recorded 90° from X in the experiment. A similar response evolution is seen in the calculated lattice spacing change under isotropic and self-hardening. It is worth noting however that whilst there is a clear effect of strain ratio under isotropic hardening by comparing the evolution of lattice spacing at 90° and 0° from X, this effect is diminished under self-hardening. This is attributed to the nature of self-hardening in which the favourably oriented slip systems dominate the evolution of lattice strain. Thus, unlike the isotropic case whereby all systems harden regardless, self-hardening is better at capturing local variations leading to more balance between both tensile axes considered. Further, Fig. 16 (a) shows that the experimental lattice spacing change lies between the calculated isotropic and self-hardening simulations. On the other hand, the simulations (self- and isotropic) initially overestimate the evolution of lattice spacing along the X-axis corresponding to the smaller applied strain, however, a good agreement is seen at 5% strain.

Under uniaxial straining shown in Fig. 17, the crystal plasticity calculations under either hardening law somewhat overestimate the experimental lattice spacing change along the loading axis at 90° from X. However, a good agreement is observed in the compressive direction i.e. 0° from X shown in Fig. 17 (b). Due to the nature of hardening, higher levels of lattice spacing are expected under isotropic compared to self-hardening. And, as described earlier, a smaller difference between isotropic and self-hardening is expected in comparison to biaxial straining shown in Fig. 16 based on the analysis shown in Appendix C.

The small differences in Figs. 14, 16 and 17 may be attributed to (1) calibration of hardening levels, (2) the superposition of the reflected beams not accounted for in the model and, (3) the tolerance of Bragg's condition specified. Points (2) and (3) require further improvement of the diffraction prediction model, though it is argued that these effects are likely to be small relative to those from a mis-representation of the hardening occurring at individual slip system level. The hardening forms adopted here are ideal and only set the extreme bounds compared to the true nature of hardening found in ferritic steel. Given the similar distributions seen under both forms of hardening, it is expected that the true hardening nature lies between these set bounds. An attempt to calibrate/improve the hardening characteristics would involve adopting mixed hardening forms such as cross hardening. That is, hardening on an active slip system results in more/less hardening on inactive systems as

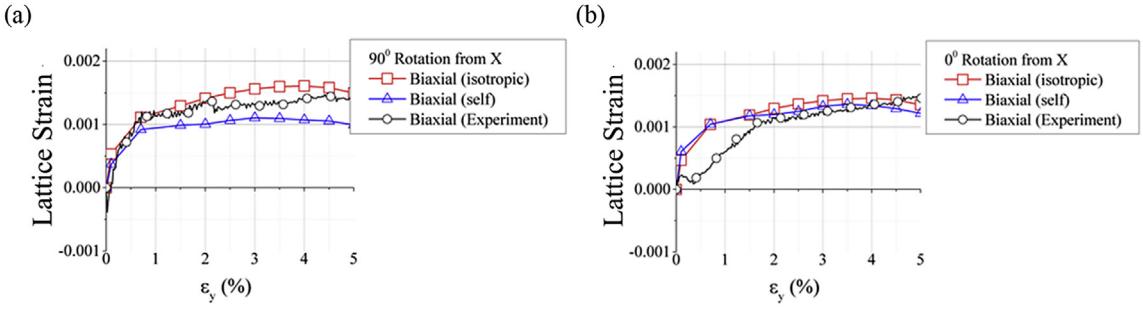

Fig. 16. Evolution of lattice strain change for texture T-2 for azimuthal sectors at $\psi = 90°$ in (a) and $\psi = 0°$ in (b) during biaxial deformation.

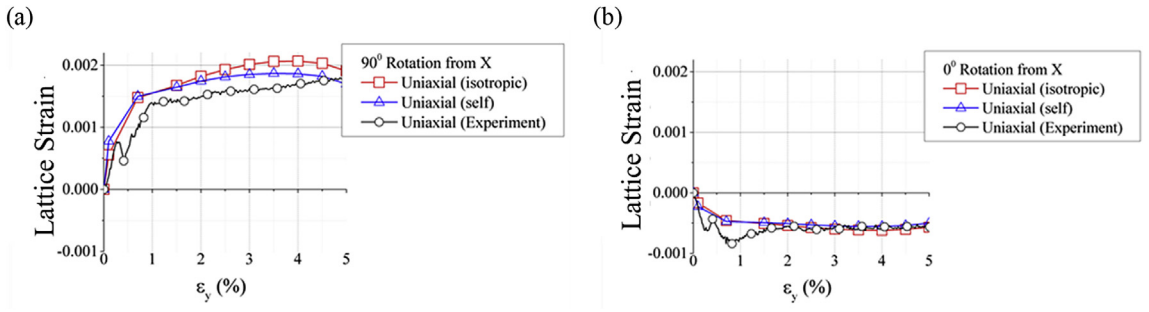

Fig. 17. Evolution of lattice strain for texture T-2 for azimuthal sectors at 90° in (a) and 0° in (b) during uniaxial deformation.

opposed to the same level under isotropic hardening or zero hardening on inactive systems under self-hardening. This form of hardening has been demonstrated in Erinosho et al. (2013b) to result in significantly different strain distributions. The incorporation of more sophisticated/complex hardening laws could have been implemented in this study, such as those that incorporate the effect of dislocation cell structure formation, as performed by Warwick et al. (2012a). The development of such laws were coupled to the features experimentally observed during certain strain-paths. In spite of the relatively simple hardening laws employed in this work, accounting for just 4 materials parameters obtained from tensile data, reasonable agreement is observed between the experimental and modelled data, without resorting to further advanced characterisation methods to inform the constitutive equations.

Despite the small differences seen by comparing experiment and simulation, it has been established that the current diffraction model accurately predicts strain path and texture dependent lattice strain distributions.

7. Conclusions

A methodology to calculate lattice strain using crystal plasticity is presented by considering grains which satisfy Bragg's condition within a 5° tolerance. Whilst this is an oversimplification of the experimental method and its inherent assumptions, it was justified to be reasonable within the context of the crystal plasticity framework adopted due to the constraint imposed on the number of grains modelled. Two forms of hardening were considered for a range of textures subjected to uniaxial and biaxial deformation.

The resulting experimentally measured polycrystal deformation maps for both strain paths considered showed good agreement with the crystal plasticity simulations. Biaxial deformation showed quite uniform lattice strain distributions regardless of texture or hardening due to the nature of straining. Uniaxial straining on the other hand showed tension on lattice planes parallel to the loading direction and compression laterally as seen in the experiment. The differences in hardening contributed to changes in lattice strain magnitude but, the overall distribution under both forms was similar. Biaxial straining influenced hardening more compared to uniaxial straining and this was attributed to the larger equivalent plastic strain rate developed under biaxial compared to uniaxial straining. Finally, the differences seen by comparing experiments with crystal plasticity simulations were attributed to calibration of hardening levels, the superposition of the diffracted beam not accounted for in this model and, the tolerance of Bragg's condition specified.

Acknowledgements

Funding has been provided by EPSRC (grant EP/I021043/1) with material and guidance from BMW-MINI gratefully acknowledged. With thanks also to the Diamond Light Source for the allocation of beamtime EE9333-1 on the I12 instrument and to Mahmoud Mostafavi, Hamidreza Abdolvand, Thomas Connolley and Christina Reinhard for their assistance during the experiment.

Appendix A. Justification of grains set size using lattice spacing evolution

Four polycrystal models each with 25 × 25 × 25 μm^3 grain size shown in Fig. A1 are incorporated with a fully random texture shown in Fig. 8 and subjected to balanced biaxial straining ($\varepsilon_Y = \varepsilon_X$). This strain ratio and texture were selected because of the expected uniform lattice spacing for all lattice plane normals in the plane of the applied strain, as shown in Fig. A2 (a). The results show that the 5 × 5 × 5 grain model shows significant fluctuations compared to the 6 × 6 × 6 grains. Increasing the model size to 8 × 8 × 8 and 10 × 10 × 10 grains, however, showed less fluctuation and approximately approached the relatively flat response expected. Whilst a larger model can be adopted, the 8 × 8 × 8 grain model was chosen due to the small differences compared to 10 × 10 × 10. This is illustrated in Fig. A2 (b) which shows the scatter associated with each model. The scatter is defined as the square of the difference between the lattice spacing distribution of each model and

its mean. Similar distributions are seen in the 8 × 8 × 8 and 10 × 10 × 10 models hence, it was assumed to be a computationally efficient model and therefore adopted in this paper.

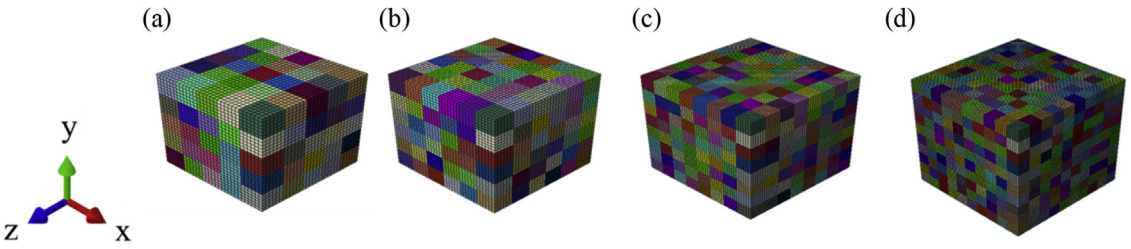

Fig. A1. The range of polycrystal models with differing number of grains (a) 5×5×5 (b) 6×6×6, (c) 8×8×8 and (d) 10×10×10 grains which are used to calibrate the simulated diffraction responses. Note that the same mesh refinement (6×6×6 elements per grain) was adopted per grain in all oligocrystal models and each grain had dimensions of 25×25×25μm^3. Note that colour denotes a region of uniform crystallographic orientation.

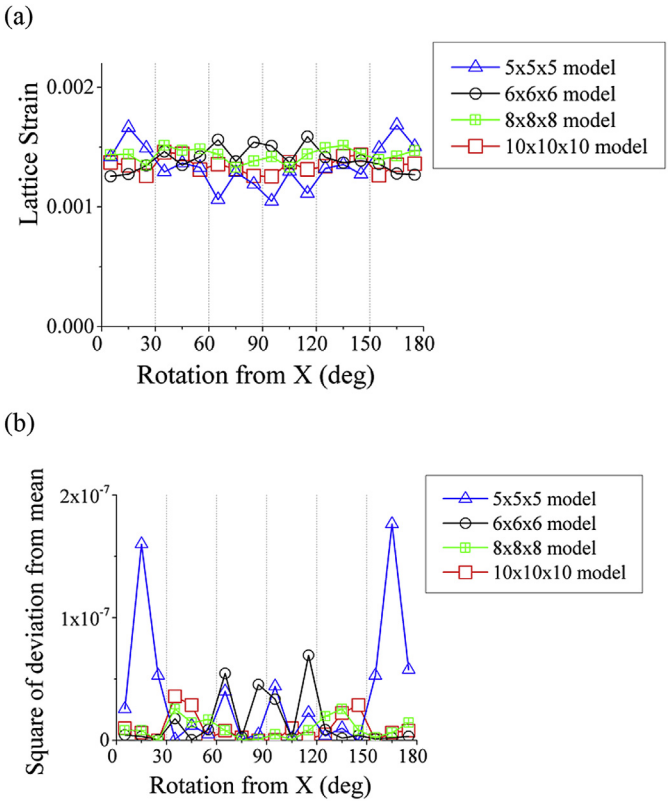

Fig. A2. (a) Evolution of lattice strain for a range of polycrystal models shown in Fig. A1 incorporated with texture T-1 shown in Fig 8 under balanced biaxial straining and (b) square of its deviation from its mean spacing in (a).

Appendix B. Justification of boundary conditions

Here, all negative surfaces are constrained to remain planar and displacement is applied to the positive X- and Y- surfaces of the polycrystal shown in Fig. 9. The positive Z-surface is also constrained to remain planar. Under uniaxial straining for example, displacement is applied to the Y- surface with the X- and Z-surfaces constrained to remain planar. However, it is also possible to adopt another boundary condition in which the positive X- and Z-surfaces are left unconstrained. The former is adopted on the basis that the polycrystal has a sufficient number of grains in the three orthogonal directions 8 × 8 × 8 such that deformation is controlled by bulk processes rather than the surface. This is illustrated in Fig. B1 which shows sections of a polycrystal deformed to an identical state under uniaxial straining with both surface constrained and unconstrained conditions. It is seen that whilst differences may be seen on the surface, both sets of boundary conditions lead to near identical plastic strain distributions within the bulk of the polycrystal; the only exceptions are very close to free surfaces. Therefore, the boundary condition surface effects are shown to be negligible and irrelevant to this study and hence those in Fig. B1 (a) are adopted.

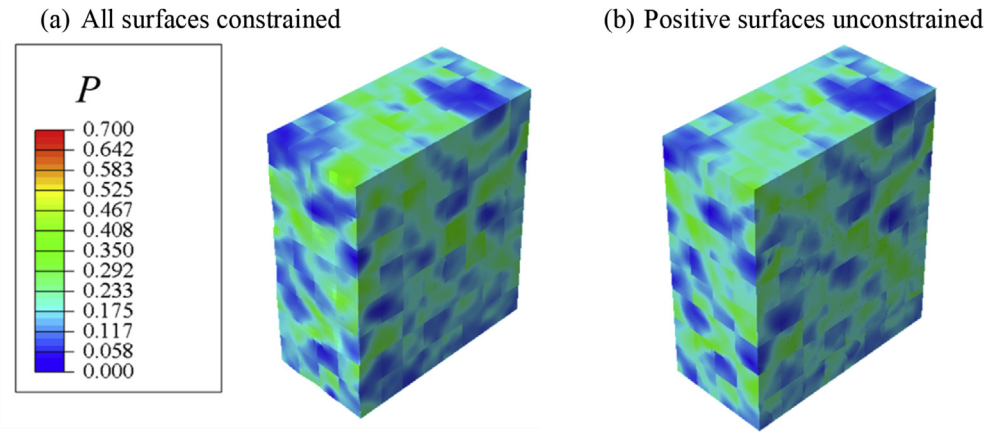

Fig. B1. Textured polycrystal subjected to uniaxial straining under two initial boundary conditions. In both cases, displacement is applied to the positive Y-surface. In (a) the positive X- and Z-surfaces are constrained to remain planar whereas they are left unconstrained in (b).

Appendix C. Influence of strain ratio on lattice strain magnitude

The equivalent plastic strain ($d\hat{\varepsilon}^p$) increment can be calculated using

$$d\hat{\varepsilon}^p = \frac{\sqrt{2}}{3}\sqrt{\left(d\hat{\varepsilon}^p_X - d\hat{\varepsilon}^p_Y\right)^2 + \left(d\hat{\varepsilon}^p_Y + d\hat{\varepsilon}^p_Z\right)^2 + \left(d\hat{\varepsilon}^p_Z + d\hat{\varepsilon}^p_X\right)^2} \tag{B1}$$

where $d\hat{\varepsilon}^p_X$, $d\hat{\varepsilon}^p_Y$ and $d\hat{\varepsilon}^p_Z$ represent the increment of plastic strain in the orthogonal X, Y and Z directions shown schematically in Fig. 9 noting that the plastic strain tensor ($\hat{\varepsilon}^p$) is given by $\hat{\varepsilon}^p = \begin{pmatrix} \hat{\varepsilon}^p_{XX} & \hat{\varepsilon}^p_{XY} & \hat{\varepsilon}^p_{XZ} \\ \hat{\varepsilon}^p_{YX} & \hat{\varepsilon}^p_{YY} & \hat{\varepsilon}^p_{YZ} \\ \hat{\varepsilon}^p_{ZX} & \hat{\varepsilon}^p_{ZY} & \hat{\varepsilon}^p_{ZZ} \end{pmatrix}$.

Consider uniaxial straining, $d\hat{\varepsilon}^p_X = d\hat{\varepsilon}^p_X$ and $d\hat{\varepsilon}^p_Y = d\hat{\varepsilon}^p_Z = -\frac{1}{2}d\hat{\varepsilon}^p_X$. Therefore, substituting into Eq. (B1), the equivalent plastic strain, $d\hat{\varepsilon}^p_{uni} = d\hat{\varepsilon}^p_X$.

Next consider biaxial straining, $d\hat{\varepsilon}^p_X = d\hat{\varepsilon}^p_Y$ and $d\hat{\varepsilon}^p_Z = -2d\hat{\varepsilon}^p_X$. Similarly, by substituting into Eq. (B1), the equivalent plastic strain, $d\hat{\varepsilon}^p_{bi} = 2d\hat{\varepsilon}^p_X$.

Since $d\hat{\varepsilon}^p_{bi} = 2d\hat{\varepsilon}^p_{uni}$, it is expected that the biaxial strain ratio will show more work hardening compared to uniaxial straining and also accounts for the more apparent differences seen due to hardening under biaxial compared to uniaxial straining.

References

Barton, N.R., Dawson, P.R., 2001. A methodology for determining average lattice orientation and its application to the characterization of grain substructure. Metall. Mater. Trans. a-Phys. Metall. Mater. Sci. 32 (8), 1967–1975.
Cihak, U., et al., 2006. Characterization of residual stresses in turbine discs by neutron and high-energy X-ray diffraction and comparison to finite element modeling. Mater. Sci. Eng. a-Struct. Mater. Prop. Microstruct. Process. 437 (1), 75–82.
Collins, D.M., et al., A synchrotron X-ray diffraction study of in situ biaxial deformation. Acta Mater.. 90(0): pp. 46–58.
Cullity, B.D. and S.R. Stock, Elements of X-ray Diffraction. third ed., New International Edition. ed. ii, 650 pages.
Dawson, P., et al., 1998. Computing residual stresses in polycrystals following plastic straining. Simul. Mater. Process. Theory, Methods Appl. 323–328.
Demir, E., et al., 2013. A computational framework for evaluating residual stress distributions from diffraction-based lattice strain data. Comput. Methods Appl. Mech. Eng. 265, 120–135.
Drakopoulos, M., et al., 2015. I12: the Joint Engineering, Environment and Processing (JEEP) beamline at diamond light source. J. Synchrotron Radiat. 22, 828–838.
Dye, D., et al., 2003. Diffraction strain measurements for the characterization of residual stresses in welds for gas turbine applications. Trends Weld. Res. Proc. 878–885.
Efstathiou, C., et al., 2010. A method for measuring single-crystal elastic moduli using high-energy X-ray diffraction and a crystal-based finite element model. Acta Mater. 58 (17), 5806–5819.
Erinosho, T.O., Dunne, F.P.E., 2014. Lattice strain distributions due to elastic distortions and GND development in polycrystals. J. Mech. Phys. Solids 67, 62–86.
Erinosho, T.O., Cocks, A.C.F., Dunne, F.P.E., 2013. Coupled effects of texture, hardening and non-proportionality of strain on ductility in ferritic steel. Comput. Mater. Sci. 80, 113–122.
Erinosho, T.O., Cocks, A.C.F., Dunne, F.P.E., 2013. Texture, hardening and non-proportionality of strain in BCC polycrystal deformation. Int. J. Plast. 50, 170–192.
FIT2D manual. 2014.
Hart, M.L., et al., 2013. Complete elliptical ring geometry provides energy and instrument calibration for synchrotron-based two-dimensional X-ray diffraction. J. Appl. Crystallogr. 46, 1249–1260.
Huang, Y., 1991. A User-material Subroutine Incorporating Single Crystal Plasticity in the Abaqus Finite Element Program. Harvard University Report, p. 178. MECH.
Korsunsky, A.M., et al., 2010. Probing deformation substructure by synchrotron x-ray diffraction and dislocation dynamics modelling. J. Nanosci. Nanotechnol. 10 (9), 5935–5950.

Lee, E.H., 1969. Elastic-plastic deformation at finite strains. J. Appl. Mech. 36 (1), 1.
Lewis, A.C., Qidwai, S.M., Geltmacher, A.B., 2010. Slip systems and initiation of plasticity in a body-centered-cubic titanium alloy. Metall. Mater. Trans. a-Phys. Metall. Mater. Sci. 41A (10), 2522–2531.
McGinty, R.D., McDowell, D.L., 2004. Application of multiscale crystal plasticity models to forming limit diagrams. J. Eng. Mater. Technol.-Trans. Asme 126 (3), 285–291.
McNelis, K.P., Dawson, P.R., Miller, M.P., 2013. A two-scale methodology for determining the residual stresses in polycrystalline solids using high energy X-ray diffraction data. J. Mech. Phys. Solids 61 (2), 428–449.
Miller, M.P., et al., 2008. Measuring and modeling distributions of stress state in deforming polycrystals. Acta Mater. 56 (15), 3927–3939.
Nervo, L., et al., 2014. Comparison between a near-field and a far-field indexing approach for characterization of a polycrystalline sample volume containing more than 1500 grains. J. Appl. Crystallogr. 47, 1402–1416.
Obstalecki, M., et al., 2014. Quantitative analysis of crystal scale deformation heterogeneity during cyclic plasticity using high-energy X-ray diffraction and finite-element simulation. Acta Mater. 75, 259–272.
Oddershede, J., et al., 2012. Measuring the stress field around an evolving crack in tensile deformed Mg AZ31 using three-dimensional X-ray diffraction. Acta Mater. 60 (8), 3570–3580.
Pagliaro, P., et al., 2009. Known residual stress specimens using opposed indentation. J. Eng. Mater. Technol.-Trans. Asme 131 (3).
Park, J.S., et al., 2013. Quantifying three-dimensional residual stress distributions using spatially-resolved diffraction measurements and finite element based data reduction. Exp. Mech. 53 (9), 1491–1507.
Peirce, D., Asaro, R.J., Needleman, A., 1983. Material rate dependence and localized deformation in crystalline solids. Acta Metall. 31 (12), 1951–1976.
Pellereau, B.M.E., et al., 2010. Finite element modelling and measurements of residual stress and phase composition in ferritic welds. Proc. Asme Press. Vessel. Pip. Conf. Vol 6 (Pts a and B), 1385–1392.
Raabe, D., Roters, F., Zhao, Z., 2002a. A texture component crystal plasticity finite element method for physically-based metal forming simulations including texture update. Pts 1–3. In: Aluminum Alloys 2002: Their Physical and Mechanical Properties, vol. 396–4, pp. 31–36.
Raabe, D., et al., 2002b. Theory of orientation gradients in plastically strained crystals. Acta Mater. 50 (2), 421–440.
Warwick, J.L.W., et al., 2012. Effect of texture on load partitioning in Ti-6Al-4V. Acta Mater. 60 (10), 4117–4127.
Warwick, J.L.W., et al., 2012. Lattice strain evolution during tensile and compressive loading of CP Ti. Acta Mater. 60 (19), 6720–6731.
Webster, P.J., et al., 2001. Synchrotron X-ray residual strain scanning of a friction stir weld. J. Strain Anal. for Eng. Des. 36 (1), 61–70.
Withers, P.J., et al., 2008. Recent advances in residual stress measurement. Int. J. Press. Vessel. Pip. 85 (3), 118–127.
Wong, S.L., et al., 2013. A framework for generating synthetic diffraction images from deforming polycrystals using crystal-based finite element formulations. Comput. Mater. Sci. 77, 456–466.
Zhao, Z., et al., 2001. Introduction of a texture component crystal plasticity finite element method for anisotropy simulations. Adv. Eng. Mater. 3 (12), 984–990.